INT. J. NUM. METH. HEAT FLUID FLOW, VOL. 5, 287–300 (1995)

EULER CALCULATIONS OF DIFFUSER FLOW FIELD, FREE JETS AND IMPINGING JETS

R. C. MEHTA†, M. J. PANDYA‡ AND T. JAYACHANDRAN‡

† *Aerodynamics Division*
‡ *Heat Transfer and Combustion Division, Vikram Sarabhai Space Centre, Trivandrum 695022, India*

ABSTRACT

Under- and over-expanded jet flows are calculated for the Euler equations. The solution procedure is based on the two-stage Runge-Kutta time-stepping scheme. The studies of the flow field structure in diffusers, free jets and impinging jets have been investigated for a range of jet-to-stream total pressure ratios and for different exit Mach numbers. The resulting flows show a complex shock-shear expansion structure with Mach discs. Numerical results are compared with available experimental data and with previously published data. An oscillating phenomenon was observed in the case of free jets operating at sonic exit Mach number and in another case of impingement of under-expanded jets on a flat plate.

KEY WORDS Euler calculations Expanded jet flows Free jets Impinging jets Diffusers

NOMENCLATURE

d	nozzle exit diameter	P_t	pitot pressure
e	internal energy	r	radial coordinate
$\mathbf{F}$	vector of x-directed fluxes	t	time
$\mathbf{G}$	vector of r-directed fluxes	T	temperature
l	distance from nozzle exit plane to the plate	$\mathbf{U}$	vector of conserved variables
M_j	exit Mach number	u, v	velocity components
P	pressure	x	axial coordinate
P_c	total pressure	Δr	radial increment
p_a	ambient pressure	Δx	axial increment
p_j	nozzle exit pressure	Δt	time increment
P_0	stagnation pressure	ρ	density
		γ	ratio of specific heats

INTRODUCTION

Diffusers, free jets and impinging jets problems find many practical applications in aerospace industries. The flow field produced by expanding jets emanating from a rocket nozzle produces very complicated flow field structures. The structures of the flow field consist of jet shocks, reflecting shocks, Mach discs, jet boundaries, slip lines, mixing regions, etc. Mechanisms for the occurrence of Mach discs in the jet are not satisfactorily available in the literature. The topic is under investigation.

0961–5539/95/040287–14$2.00

Received September 1993
Revised March 1994

Solution of the parabolised Navier-Stokes equations using shock capturing methods for single- or two-phase, steady, supersonic jets has been reported by Dash and Wolf[1]. The solution of the unsteady Euler equations for obtaining the flow field of inder-expanded, two-dimensional, free jets was carried out by Sinha *et al.*[2]. Sommerfeld[3] and Ishii and Omeda[4] obtained results for a free jet with and without particles by solving the unsteady, inviscid equations.

Due to the highly nonlinear nature of jet flows, the Euler equations are the lowest order approximation that gives a reasonable model for the fluid mechanics of these flows. In the present analysis, the flow field inside diffusers, free jets and impinging jets are analysed by solving the two-dimensional/axisymmetric Euler equations. The main aim of the present analysis is to compare the numerical results with experimental data in order to undertake validation tests.

GOVERNING EQUATIONS

Effects of turbulent mixing, which can substantially alter the flow far downstream of the nozzle, are neglected in this study. The assumption of large Reynolds number is relatively safe, except for the region near the jet boundary, where substantial mixing takes place[5]. The equations solved are the Euler equations describing the flow of an inviscid, compressible fluid. To capture shocks and discontinuities, the Euler equations are written in conservation form as:

$$\frac{\partial \mathrm{U}}{\partial t}+\frac{\partial \mathrm{F}}{\partial x}+\frac{\partial \mathrm{G}}{\partial r}+\mathrm{H}=0 \tag{1}$$

where,

$$\mathrm{U}=r^m\begin{bmatrix}\rho\\ \rho u\\ \rho v\\ \rho e\end{bmatrix},\quad \mathrm{F}=r^m\begin{bmatrix}\rho u\\ \rho u^2+p\\ \rho uv\\ (\rho e+p)u\end{bmatrix},\quad \mathrm{G}=r^m\begin{bmatrix}\rho v\\ \rho uv\\ \rho v^2+p\\ (\rho e+p)v\end{bmatrix},\quad \mathrm{H}=\begin{bmatrix}0\\ 0\\ mp\\ 0\end{bmatrix}$$

and

$$m=0 \quad \text{for planar case}$$

$$m=1 \quad \text{for axisymmetric case}$$

The total internal energy e is given by:

$$e=\frac{p}{\rho(\gamma-1)}+\frac{1}{2}(u^2+v^2) \tag{2}$$

with the speed of sound:

$$a=\sqrt{\frac{\gamma p}{\rho}} \tag{3}$$

where the specific heat ratio γ is taken as a constant for all the calculations reported here.

An integral form of equation (1), over a finite volume fixed in time, is:

$$\frac{\partial}{\partial t}\int_\Omega \mathrm{U}d\Omega+\int_\Gamma(\mathrm{F}dr-\mathrm{G}dx)+\int_\Omega Hd\Omega=0 \tag{4}$$

where Ω refers to the volume with boundary Γ. The computational domain is divided into a finite number of quadrilateral cells. The conservative variables within each cell are calculated by their average value at the cell centre and such quantities are denoted by suffices (i,j). We obtain a system of ordinary differential equations by applying (4) separately to each cell. These equations have the form:

$$\frac{d(\Delta A_{ij}\mathbf{U}_{ij})}{dt} + Q_{ij} - D_{ij} = 0 \tag{5}$$

where ΔA is the cell volume, and **Q** represents the net absolute flux out of the cell. The fluxes are computed at cell faces by averaging the cell-centre fluxes on adjacent sides. The finite volume scheme (5) constructed in this manner reduces to a central-difference scheme and is second-order accurate in space provided that the mesh is smooth enough. The vector **D** is the local dissipation flux required to eliminate spurious oscillations typical to central difference algorithms.

ARTIFICIAL DISSIPATION

The cell centered spatial discretization method is nondissipative, so that any truncation and round-off errors are not damped in time, and oscillations may be present in steady-state solution. In order to eliminate these oscillations, dissipative terms D are added to (5). The dissipative term consists of the following operators in each direction:

$$D\mathbf{U} = D_x\mathbf{U} + D_r\mathbf{U} \tag{6}$$

The dissipative fluxes in each direction are given by:

$$D_x\mathbf{U} = d_{i+1/2,j} - d_{i-1/2,j} \tag{7a}$$

$$D_r\mathbf{U} = d_{i,j+1/2} - d_{i,j-1/2} \tag{7b}$$

$$d_{i+1/2,j} = \frac{(\Delta A)_{i+1/2,j}}{\Delta t}\{\varepsilon^{(2)}_{i+1/2,j}(\mathbf{U}_{i+1,j} - \mathbf{U}_{i,j}) - \varepsilon^{(4)}(\mathbf{U}_{i+2,j} - 3\mathbf{U}_{i+1,j} + 3\mathbf{U}_{i,j} - \mathbf{U}_{i-1,j})\} \tag{8}$$

of second- and fourth-order in the conserved variables, **U**. The term $d_{i,j+1/2}$, $d_{i,j-1/2}$, etc., are calculated in an analogous manner. The numerical value of the constant ε influences the solution accuracy and, hence, must be carefully calculated. The way that these ε coefficients are chosen is to adapt them to the local flow gradients. The second order coefficient $\varepsilon^{(2)}$ calculated as:

$$\varepsilon^{(2)} = \max(\nu_{i+1,j}, \nu_{i,j}) \tag{9}$$

where

$$\nu_{i,j} = \kappa^{(2)}\frac{|p_{i+1,j} - 2p_{i,j} + p_{i-1,j}|}{|p_{i+1,j} + 2p_{i,j} + p_{i-1,j}|} \tag{10}$$

where $\kappa^{(2)}$ is a constant. However, the outcome is that $\varepsilon^{(2)}$ is positive, of order $(\Delta x)^2$, and proportional to the second difference of pressure. It suppresses the oscillations around the shock. Fourth-order dissipation is added everywhere in the flow domain where the solution is smooth but are "switch-off" in the region of shock waves. The term involving second order differences is "switch-on" to damp oscillations near shock waves. The $\varepsilon^{(4)}$ is set to

$$\varepsilon^{(4)}_{i+1/2,j} = \max\{(0, (\kappa^{(4)} - \varepsilon^{(2)}_{i+1/2,j})\} \tag{11}$$

where $\kappa^{(4)}$ is another constant. The scaling $[(\Delta A_{i+1/2,j})/\Delta t]$ in (8) confirms to the inclusion of the cell volume in the dependent variables of (5). Since Equation (8) contains undivided differences, it follows that if $\varepsilon^{(2)} = O(\Delta x)^2$ and $\varepsilon^{(4)} = O(1)$, then the added terms are of $O(\Delta x)^3$, as will be the case in the regions where the flow is smooth. Near a shock wave $\varepsilon^{(2)} = O(1)$, and the scheme behaves locally as a first-order-accurate scheme. The recommended values of $\kappa^{(2)}$ are in the range of 1 to 2, and $\kappa^{(4)}$ in the range of 1/32 to 1/256. In the present numerical analysis, various values of $\kappa^{(2)}$ and $\kappa^{(4)}$ are tried in order to control the numerical oscillations. The values of $\kappa^{(2)}$ and $\kappa^{(4)}$ are selected as 2.0 and 1/32, respectively.

RUNGE-KUTTA TIME-STEPPING SCHEME

The time-dependent governing equations (5) are integrated numerically by means of the classical second-order Runge-Kutta method[6]. Suppressing the subscripts (i, j) in (5), the following sequence of operations is used to obtain U at the time level $n+1$ time level:

$$\begin{aligned} U^{(0)} &= U^{n} \\ U^{(1)} &= U^{(0)} - \frac{\Delta t}{2}(Q^{(0)} - D^{(0)}) \\ U^{(2)} &= U^{(0)} - \Delta t(Q^{(1)} - D^{(0)}) \\ U^{n+1} &= U^{(2)} \end{aligned} \tag{12}$$

The dissipative terms are frozen at their values in the first stage. Here, only two stages are used, giving second-order accuracy in time. The scheme is stable for a Courant number $\leqslant 1$. The time-step corresponds to a lower Courant number than that directed by linear stability.

BOUNDARY CONDITIONS

The boundary conditions are enforced by using the idea of image cells at the boundaries. In these, the flow properties are set according to the type of boundaries, and then a Riemann solver is applied to compute the flux across these boundaries.

For a solid wall, the flow properties in the image cell are taken as those of the adjacent cell boundary cell, except that the normal component of the velocity is reflected to ensure the

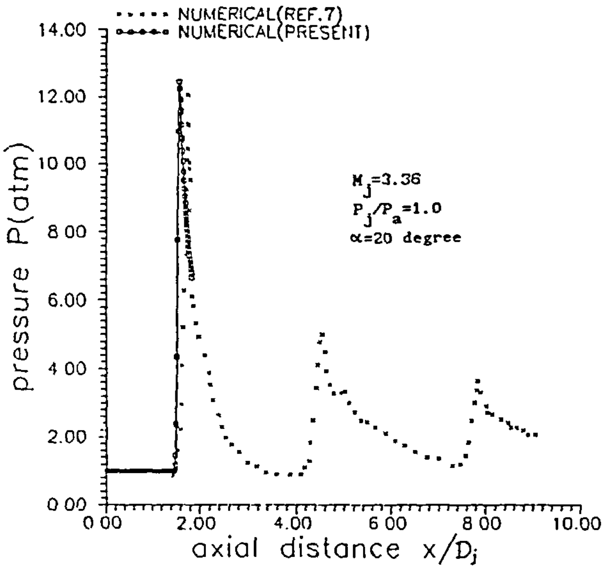

Figure 1 Centre line pressure profile

impenetrability condition. The image cell is taken while applying the symmetry condition in case of axisymmetric flow.

At the subsonic *outlet boundary*, the *pressure* is imposed whereas the remaining flow properties are extrapolated. For supersonic outflow, all of the properties in the cell are extrapolated from the adjacent interior cells.

At inlet boundaries, the total pressure and temperature, as well as the flow angle are imposed for a subsonic flow. The static pressure is taken from the neighbouring interior cell. For a supersonic inlet, all of the flow properties are imposed.

RESULTS AND DISCUSSION

The above numerical algorithm is used to solve diffuser flow fields, free jets and impinging jets problems. Extensive numerical studies have been performed for various grid sizes. However, the grid size mentioned in the tables is achieved after a grid independent check was done. The computations were performed on an i860 based work-station.

Diffuser flow field analysis

The following test cases were considered in the numerical simulations:

test	M_j	p_j/p_a	P_0/p_a	grid size	Reference
1	3.36	1.0	93.5	183 × 61	7
2	1.00	25.76	49.1	107 × 47	8
3	5.00	363.0	15000	107 × 41	9
4	5.00	485.0	20000	107 × 41	9
5	5.00	606.0	25000	107 × 41	9

In test case 1, the ducted gas passes through a series of shocks. The expanding flow has an inlet condition of $M_\infty = 3.36$, and $p_a = 1$ atm. At $x/D_j = 0$, the top wall is turned down 20 degrees, then turned back parallel to the plane of symmetry at $x/D_j = 0.825$. The computed centre line pressure distribution inside the two-dimensional duct compares well with experimental data[7] as shown in *Figure 1.* The isobar contours depict a series of shocks in *Figure 2.*

Test case 2 is taken from Reference 8 in which the flow expands in a tube. The inlet flow conditions are $M_j = 1.0$, $p_j/p_a = 25.76$ and $p_c/p_a = 49.1$. *Figure 3* shows a comparison between our numerical prediction and PHOENICS results[8]. It can be observed from the figure that the level of pressure in the tube was reasonably well predicted but oscillations are found downstream of the tube. A similar observation was also pointed out by Smith[8].

Test cases 3, 4 and 5 correspond to highly under-expanded free jets impinging upon an adjacent surface[9]. The test conditions are $M_j = 5.0$, $p_c/p_a = 15$, 20 and 25 × 10^4, and $p_j/p_a = 363$, 485 and 606. The distance from the plate to the nozzle axis is 2.0. The ratios of static to ambient pressure (p_j/p_a) vs. nondimensional distance (x/D_j) are plotted in *Figures 4, 5* and *6.* It can be observed from the pressure distribution that the experimental data are matched very well up to the

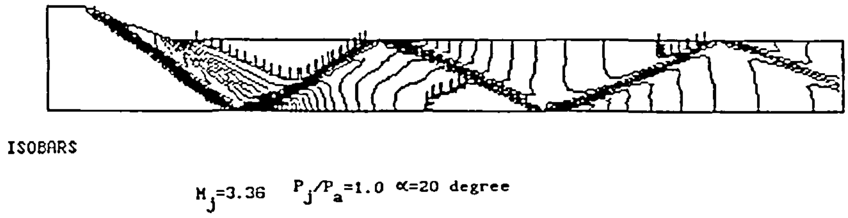

Figure 2 Isobars

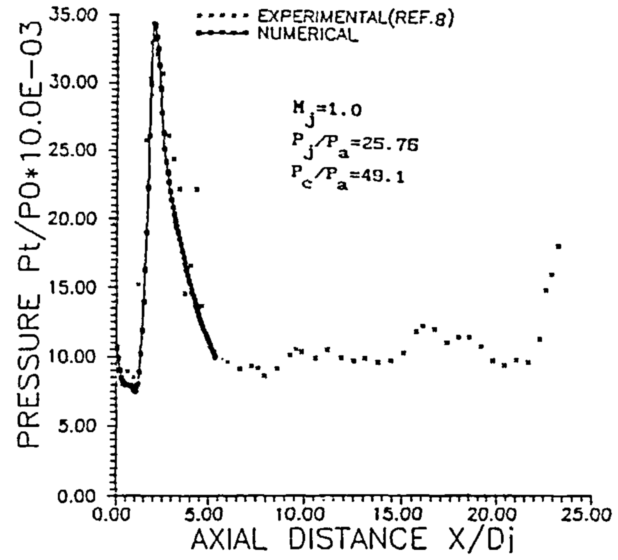

Figure 3 Centre line pressure profile

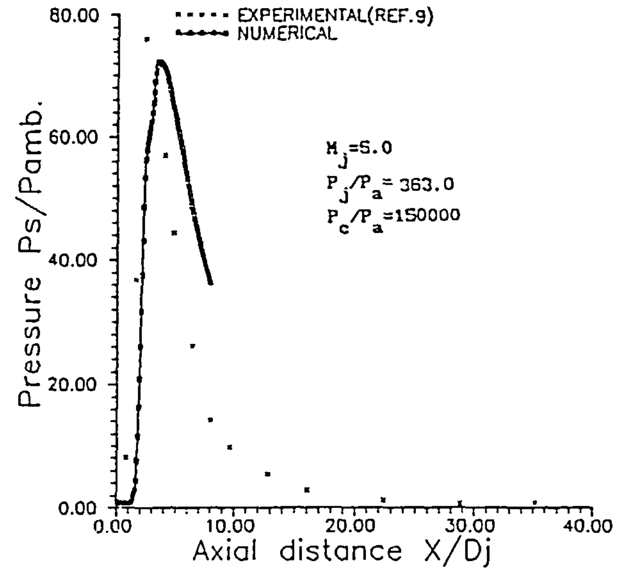

Figure 4 Pressure distribution on plate

impingement point. It is also observed from the figures that the ratio of the impingement to ambient pressure increases from 76 to 130 as p_j/p_a is increased from 363 to 606. There is disagreement after the impingement point which is attributed to viscous effects. *Figure 7* shows isobars and isoMach contours for the test case 5. It can be seen from the contour plots that the incident and reflected shocks are well captured. The flow field features indicate that the plume boundary shock strikes on the adjacent surface and forms an oblique impingement shock.

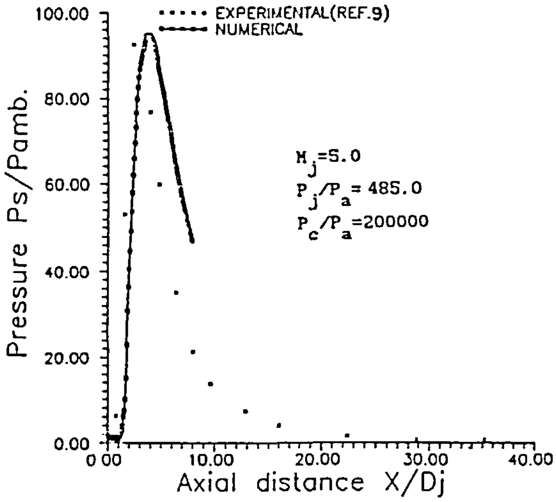

Figure 5 Pressure distribution on plate

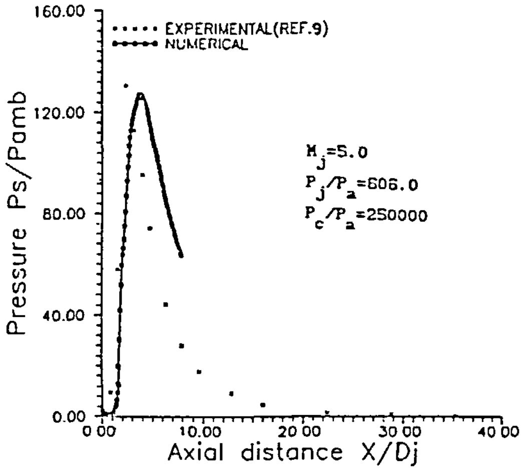

Figure 6 Surface pressure profile on plate

Free jets flow field analysis

The following cases were solved numerically for free jets:

test	M_j	p_j/p_a	p_0/p_a	grid size	Reference
6	1.0	5.28	10.0	270 × 51	10
7	1.0	7.92	15.0	270 × 51	10
8	1.0	10.57	20.0	270 × 51	10
9	2.0	1.445	4.87	145 × 41	11
10	2.20	1.2	47.7	161 × 41	12
11	2.20	0.8	47.7	161 × 41	12

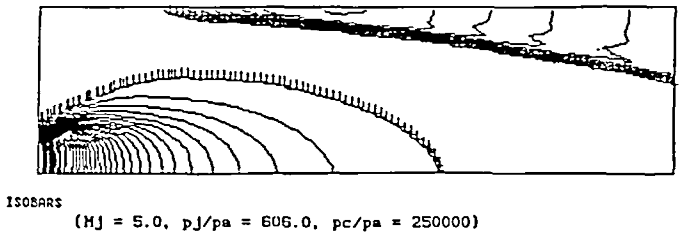

Figure 7a Isobars

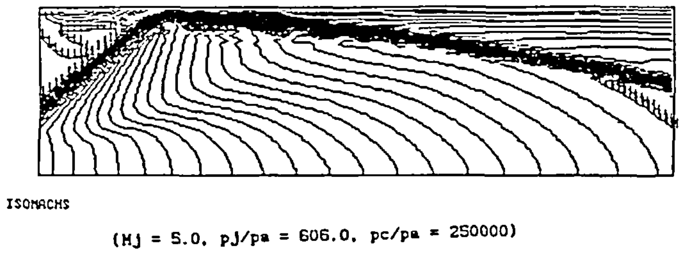

Figure 7b IsoMach lines

Test cases 6, 7 and 8 are taken from the experimental work of Cobald[10]. Numerical analysis was carried out for a free air jet at $M_j = 1.0$ at three different ambient conditions. *Figures 8, 9* and *10* show the jet centre line nondimensional pitot pressure vs. $x/(0.5D_j)$. The comparison between computed and experimental results shows disagreement between them. However, the disagreement between them decreases as p_j/p_a is increased. An oscillating phenomenon was observed around the convergence criterion, i.e., $\max|\rho^{l+1} - \rho^l| \leqslant 10^{-5}$, where l is an iteration index. The reason for the disagreement is due to a fluctuating phenomenon around the steady state solution. An identical observation was seen by Ishii and Umeda[4] while analysing free jets problem, using a piecewise linear interpolation method in conjunction with the method of characteristics. *Figure 11* shows the Mach contour plots. It can be seen from the plot that all the essential flow field features are captured such as the jet boundaries, the Mach disc and the barrel shock.

Figure 12 shows results for test condition 9. The pressure distribution along the centre line is in good agreement with experimental data[11].

Test conditions 10 and 11 correspond to under- and over-expanded supersonic free jet conditions, respectively. Experiments were conducted by Prasad[12] for a nozzle exit Mach number $M_j = 2.2$ and $p_j/p_a = 1.2$ and 0.8. The exit diameter of the nozzle was 23 mm and the nozzle angle was 15 degrees. The comparison between the numerical and experimental[12] results is depicted in *Figure 13*; good agreement between them is observed. *Figure 14* displays density and Mach contour plots for under-expanded free jets. The shock cells, jet boundaries and Mach disc are visible in the density contour plots. The overall flow field features of the supersonic free jets is well captured by the present numerical scheme.

Jet impinging flow field analysis

The following test cases were analysed numerically for impinging jets:

test	M_j	l/D_j	P_0/p_a	grid size	Reference
12	1.0	2.0	3.0	41 × 61	13
13	1.0	2.5	3.0	41 × 61	13

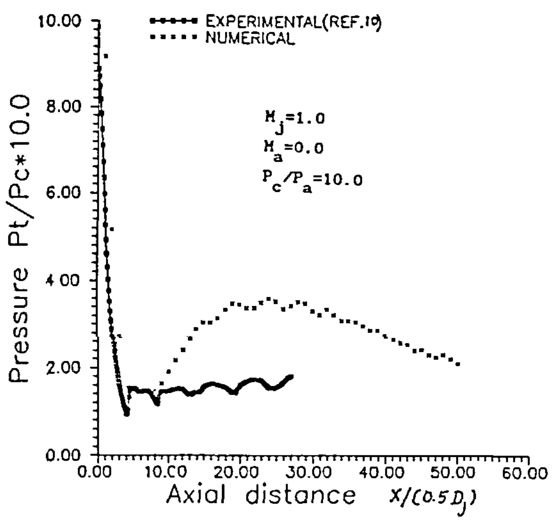

Figure 8 Centre line pressure distribution

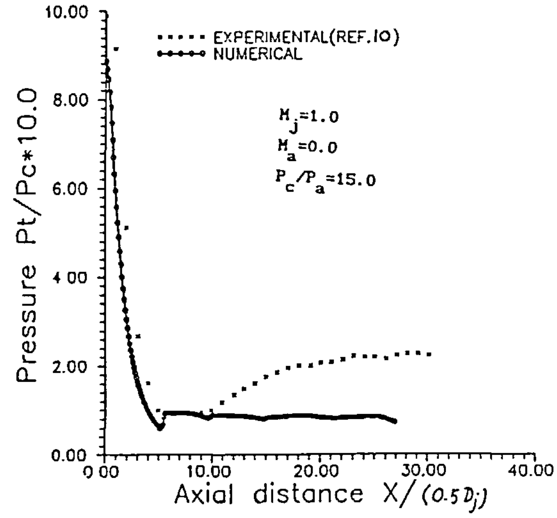

Figure 9 Centre line pressure distribution

When a surface is placed in the path of sonic jets, at some point on the surface there exist a stagnation region. In bringing the flow to rest, deceleration to subsonic velocities occurs, thus producing shock waves. Different parts of the impinging flow field have different shock structures. Such a complex flow field is analysed in test cases 12 and 13. *Figure 15* shows comparisons between experimental and numerical results for $p_0/p_a = 3.0$ at $l/D_j = 2.5$. The numerical and experimental data[13] exhibit good agreement. As can be observed from *Figure 15*, the numerical results show that the density along the axis of symmetry of the jet drops from its value at the nozzle exit plane to its minimum value at $x/D_j = 0.8$ and reaches its maximum value at $x/D_j = 1.3$ downstream of the oblique shock wave. The density decreases again and reaches its minimum

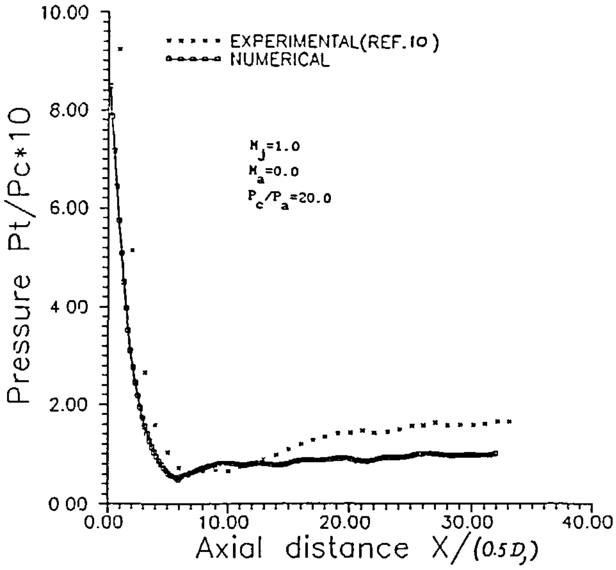

Figure 10 Centre line pressure distribution

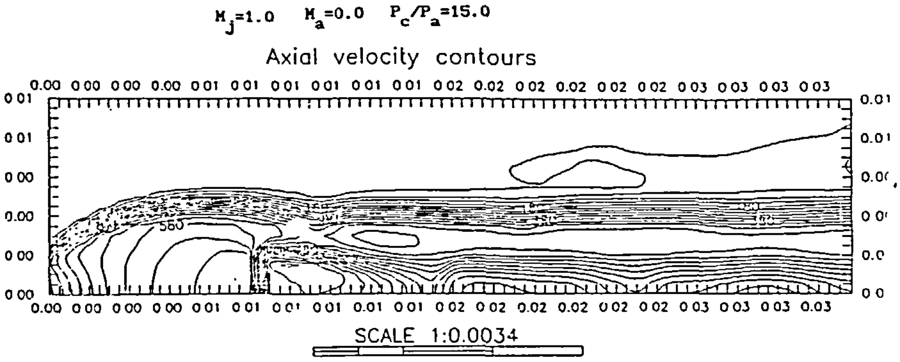

Figure 11 Mach contours

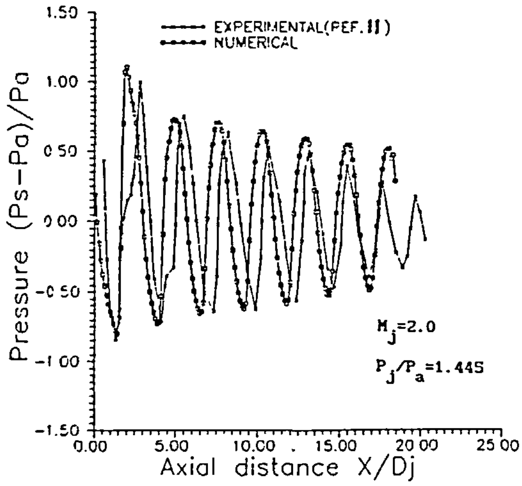

Figure 12 Centre line pressure distribution

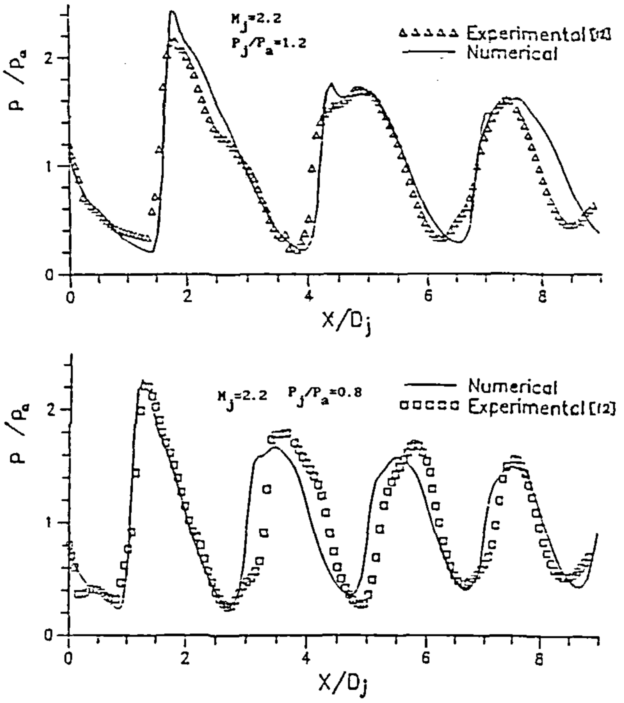

Figure 13 Centre line pressure variation

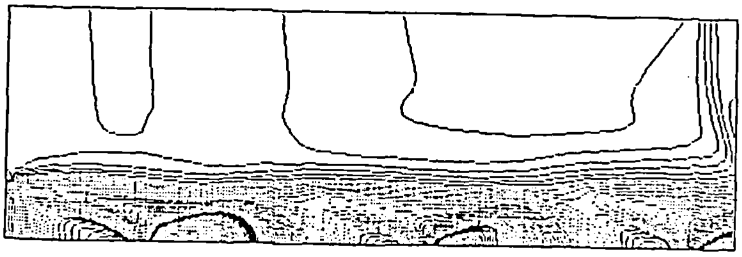

DENSITY CONTOURS

$M_j=2.2$ $P_j/P_a=1.2$

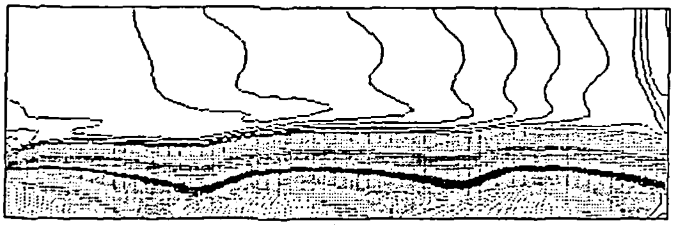

MACH CONTOURS

Figure 14 Mach contours

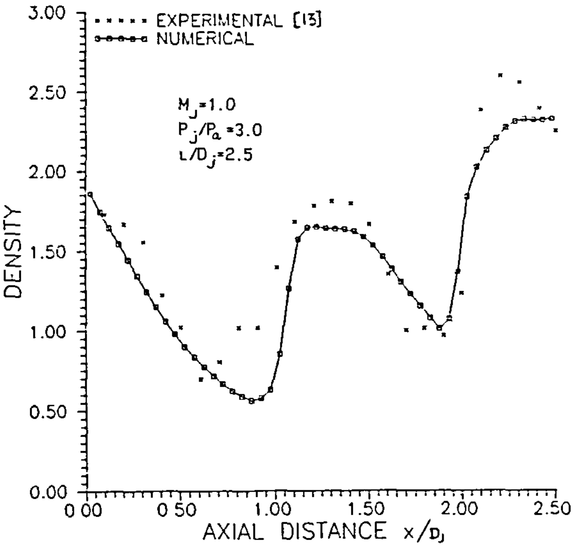

Figure 15 Centre line density distribution

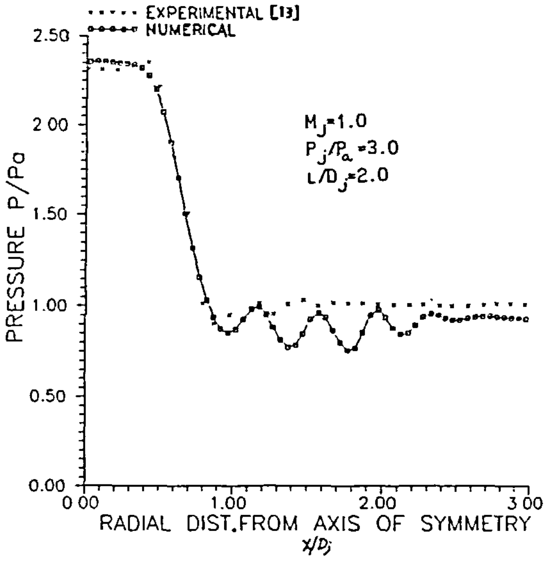

Figure 16 Surface pressure profile on plate

value at $x/D_j = 1.8$, upstream of the shock which is formed in front of the flat plate. *Figures 16* and *17* show the pressure distribution on the flat plate obtained from the numerical calculations for $l/D_j = 2.0$ and 2.5. It can be seen from the figures that the numerical results compare well with experimental data[13]. As the distance between the nozzle exit plane and the plate l/D_j is increased from 2.0 to 2.5, the pressure ratio p_j/p_a decreases from 2.66 to 2.35. The pressure distribution on the plate surface fluctuates about the ambient pressure. It might be worthwhile mentioning here that the large scale flow characteristics of the jet remain unchanged. Although

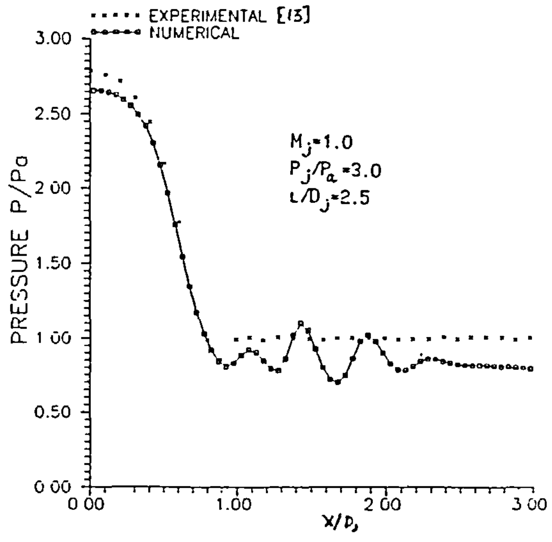

Figure 17 Surface pressure profile

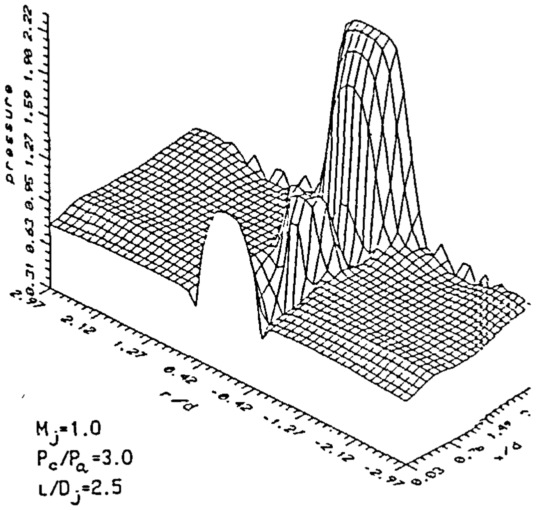

Figure 18 (a) Pressure distribution

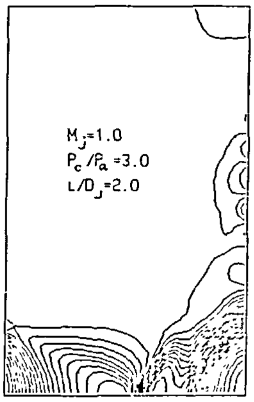

Figure 18 (b) Isobars

they show a kind of oscillating phenomenon around the convergence criterion as mentioned earlier. *Figure 18a* shows the pressure distribution of the entire flow field between the nozzle exit plane and the plate obtained numerically for $p_c/p_a = 3.0$ and $1/D_j = 2.5$. The jet expands from the high pressure at the nozzle exit plane to the lowest pressure where the oblique shock waves cross the ket axis. *Figure 18b* shows isobars for $p_c/p_a = 3.0$ and $1/D_j = 2.0$. The isobars plot shows the Mach disc position.

CONCLUSIONS

A finite volume discretization is used to solve the Euler equations in conjunction with a two-stage Runge-Kutta method. Numerical solutions are obtained for diffusers, free jets and impinging jets. Many test cases were performed to analyse the numerical results. Different grid arrangements were used in each test case in order to get grid independent numerical results. All the flow field features are captured by the present numerical analysis. Agreement and disagreement with experimental results are discussed. A fluctuation in axial pressure is found in the case of free jets issuing at sonic exit Mach number from a nozzle. In the case of impingement of under-expanded jets on a flat plate, the surface pressure fluctuates about the ambient pressure.

REFERENCES

1 Dash, S. M. and Wolf, D. F. Fully-coupled analysis of jet mixing problems. Part 1: Shock-capturing model, SCIPVIS, NASA CR 3761 (1984)
2 Sinha, R., Zakkay, V. and Erdos, J. Flow field analysis of plumes of two-dimensional under-expanded jets by a time-dependent method, *AIAA J.*, 9, 2363–2370 (1971)
3 Sommerfeld, M. Expansion of a gas/particle mixture in supersonic free jet flow. *Z. Flugwiss Wellraumfrsch*, **11**, 87–96 (1987)
4 Ishii, R. and Umeda, Y. Free-jet flows of gas-particle mixtures, AIAA paper No. 86-1317, *AIAA/ASME 4th Joint Thermophysics Conf.*, Boston, June 2–4 (1986)
5 Adamson, T. C., Jr. The structure of the rocket exhaust plume without reaction at various altitudes, in *Supersonic Flow, Chemical Processes and Radiative Transfer*, Pergamon Press (1964)
6 Jameson, A., Schmidt, W. and Turkel, E. Numerical solution of the Euler equations by finite volume methods using Runge-Kutta time-stepping schemes, *AIAA paper No. 81-1259* (1981)
7 Dash, S. M., Thrope, R. D. and Pergament, H. S. Inclusion of gas/particle interactions in a shock-capturing model for nozzle and exhaust plume flows, *AIAA paper No. 79-1288*, Las Vegas (1979)
8 Smith, A. G. Use of PHOENICS for prediction of rocket exhaust flows, *Third Int. PHOENICS Users Conf.*, Dubrovnik (1989)
9 Vick, A. R. and Andrews, E. H. An experimental investigation of highly underexpanded free jets impinging upon a parallel flat plate, NASA TN-D 2326 (1964)
10 Cobald, T. J. The impingement of under-expanded axisymmetric rocket motor exhaust and cold jets on flat plates, *PhD Thesis*, Department of Aeronautical Engineering, University of Bristol, UK (1985)
11 Dash, S. M. and Thrope, R. D. A shock capturing model for the analysis of steady supersonic one- and two-phase flows, *AIAA paper No. 80-1254 (1980)*
12 Prasad, J. K. Experimental and numerical studies of free jets and impinging jets, *PhD Thesis*, Indian Institute of Technology, Madras (1993)
13 Iwamoto, J. Impingement of under expanded jets on a flat plate, *ASME J. of Fluids Eng.*, **112**, 179–184 (1990)